PASJ: Publ. Astron. Soc. Japan **64**, 13, 2012 February 25

A Spectral Study of the Black Hole Candidate XTE J1752−223 in the High/Soft State with MAXI, Suzaku, and Swift

Satoshi NAKAHIRA,[1] Shu KOYAMA,[2] Yoshihiro UEDA,[3] Kazutaka YAMAOKA,[4] Mutsumi SUGIZAKI,[1] Tatehiro MIHARA,[1] Masaru MATSUOKA,[1] Atsumasa YOSHIDA,[4] Kazuo MAKISHIMA,[1,5] Ken EBISAWA,[6] Aya KUBOTA,[7] Shin'ya YAMADA,[8] Hitoshi NEGORO,[9] Kazuo HIROI,[3] Masaki ISHIKAWA,[10] Nobuyuki KAWAI,[11] Masashi KIMURA,[12] Hiroki KITAYAMA,[12] Mitsuhiro KOHAMA,[13] Takanori MATSUMURA,[14] Mikio MORII,[11] Motoki NAKAJIMA,[15] Motoko SERINO,[1] Megumi SHIDATSU,[3] Tetsuya SOOTOME,[1,7] Kousuke SUGIMORI,[11] Fumitoshi SUWA,[9] Hiroshi TOMIDA,[13] Yoko TSUBOI,[14] Hiroshi TSUNEMI,[12] Shiro UENO,[13] Ryuichi USUI,[11] Takayuki YAMAMOTO,[1,9] Kyohei YAMAZAKI,[14] Makoto S. TASHIRO,[2] Yukikatsu TERADA,[2] and Hiromi SETA[2]

[1]*MAXI team, Institute of Physical and Chemical Research (RIKEN), 2-1 Hirosawa, Wako, Saitama 351-0198*
[2]*Department of Physics, Saitama University, 255 Shimo-Okubo, Sakura-ku, Saitama 338-8570*
[3]*Department of Astronomy, Kyoto University, Oiwake-cho, Sakyo-ku, Kyoto 606-8502*
[4]*Department of Physics and Mathematics, Aoyama Gakuin University, 5-10-1 Fuchinobe, Chuo-ku, Sagamihara 252-5258*
[5]*Department of Physics, The University of Tokyo, 7-3-1 Hongo, Bunkyo-ku, Tokyo 113-0033*
[6]*Department of Space Science Information Analysis, Institute of Space and Astronautical Science (ISAS), Japan Aerospace Exploration Agency (JAXA), 3-1-1 Yoshinodai, Chuo-ku, Sagamihara 252-5210*
[7]*Department of Electronic Information Systems, Shibaura Institute of Technology, 307 Fukasaku, Minuma-ku, Saitama 337-8570*
[8]*High Energy Astrophysics Laboratory, Institute of Physical and Chemical Research (RIKEN), 2-1 Hirosawa, Wako, Saitama 351-0198*
[9]*Department of Physics, Nihon University, 1-8-14 Kanda-Surugadai, Chiyoda-ku, Tokyo 101-8308*
[10]*School of Physical Science, Space and Astronautical Science, The Graduate University for Advanced Studies (Sokendai), 3-1-1 Yoshinodai, Chuo-ku, Sagamihara 252-5210*
[11]*Department of Physics, Tokyo Institute of Technology, 2-12-1 Ookayama, Meguro-ku, Tokyo 152-8551*
[12]*Department of Earth and Space Science, Osaka University, 1-1 Machikaneyama, Toyonaka, Osaka 560-0043*
[13]*ISS Science Project Office, Institute of Space and Astronautical Science (ISAS), Japan Aerospace Exploration Agency (JAXA), 2-1-1 Sengen, Tsukuba, Ibaraki 305-8505*
[14]*Department of Physics, Chuo University, 1-13-27 Kasuga, Bunkyo-ku, Tokyo 112-8551*
[15]*School of Dentistry at Matsudo, Nihon University, 2-870-1 Sakaecho-nishi, Matsudo, Chiba 101-8308*

(Received 2011 July 25; accepted 2011 September 6)

Abstract

We report on an X-ray spectral analysis of the black hole candidate XTE J1752−223 in the 2009–2010 outburst, utilizing data obtained with the MAXI/Gas Slit Camera (GSC), the Swift/XRT, and Suzaku, which work complementarily. As already reported by Nakahira et al. (2010, PASJ, 62, L27), MAXI monitored the source continuously throughout the entire outburst for about eight months. All of the MAXI/GSC energy spectra in the high/soft state, lasting for 2 months, are well represented by a multi-color disk plus power-law model. The innermost disk temperature changed from ~ 0.7 keV to ~ 0.4 keV and the disk flux decreased by an order of magnitude. Nevertheless, the innermost radius is constant at $\sim 41\ D_{3.5}(\cos i)^{-1/2}$ km, where $D_{3.5}$ is the source distance in units of 3.5 kpc and i the inclination. The multi-color disk parameters obtained with the MAXI/GSC are consistent with those with the Swift/XRT and Suzaku. The Suzaku data also suggest a possibility that the disk emission is slightly Comptonized, which could account for broad iron-K features reported previously. Assuming that the obtained innermost radius represents the innermost stable circular orbit for a non-rotating black hole, we estimate the mass of the black hole to be $5.51 \pm 0.28\ M_\odot\ D_{3.5}(\cos i)^{-1/2}$, where the correction for the stress-free inner boundary condition and color hardening factor of 1.7 are taken into account. If the inclination is less than 49°, as suggested from radio monitoring of transient jets, and the soft-to-hard transition in 2010 April occurred at 1%–4% of Eddington luminosity, the fitting of the Suzaku spectra with a relativistic accretion-disk model derives constraints on the mass and the distance to be 3.1–55 $M_\odot$ and 2.3–22 kpc, respectively. This confirms that the compact object in XTE J1752−223 is a black hole.

Key words: accretion disks — black hole physics — stars: individual (XTE J1752−223) — X-rays: stars

1. Introduction

Galactic black hole candidates (BHCs) show various states characterized by their spectral shapes, temporal properties, and luminosities. They mostly take two major states, the "low/hard state" and the "high/soft state", which are referred to as "the hard X-ray state" and "the thermal dominant state", respectively, in a more recent classification (see McClintock et al.

2009 and references therein), since the state of a BHC is not always determined by the X-ray luminosity alone. In the low/hard state, the X-ray energy spectra are dominated by a power-law component with a photon index of ~ 1.7 and a high-energy cutoff at ~ 100 keV that shows strong short-time variability (Grove et al. 1998). They can be explained by thermal Comptonization of soft photons from the accretion disk by hot plasmas with a temperature of $\sim 10^{10}$ K (e.g., Makishima et al. 2008; Takahashi et al. 2008; Shidatsu et al. 2011a). In a typical outburst of a transient BHC, it generally exhibits a spectral transition from the low/hard to the high/soft state through the intermediate (or very high) state when the luminosity reaches $\sim 10\%$ of the Eddington limit. The X-ray spectra in the high/soft state are characterized by an ultra-soft component that is considered to originate from an optically-thick and geometrically-thin accretion disk (so called "standard disk": Shakura & Sunyaev 1973). This emission can be successfully described by the multi-color disk (MCD) model (Mitsuda et al. 1984; Makishima et al. 1986) with an innermost temperature of ~ 1 keV. An important signature in the high/soft state is that the innermost radius ($r_{\rm in}$) of the accretion disk is kept constant, independent of the flux or innermost disk temperature (e.g., Tanaka & Shibazaki 1996). Hence, it is believed that $r_{\rm in}$ reflects the innermost stable circular orbit (ISCO), which is determined through general relativity by the mass and angular momentum of the black hole; the radius of the ISCO for a non-spinning black hole is $6\,R_{\rm g}$ ($R_{\rm g} \equiv GM/c^2$ is the gravitational radius, where G, M, c are the gravitational constant, black hole mass, and light velocity, respectively). By assuming the obtained innermost $r_{\rm in}$ to the ISCO, the black hole mass can be estimated from the X-ray spectrum alone for a given spin parameter.

XTE J1752−223 was first discovered with the Proportional Counter Array (PCA) onboard Rossi X-ray Timing Explorer (RXTE) on 2009 October 23 (MJD 55127) during a Galactic bulge scan observation (Markwardt et al. 2009). The Gas Slit Camera (GSC) onboard Monitor of All-sky X-ray Image (MAXI: Matsuoka et al. 2009) detected the source simultaneously (Nakahira et al. 2009). As described in Nakahira et al. (2010, hereafter Paper I), MAXI continuously monitored the source during the entire outburst until 2010 June. The MAXI light curves and hardness–intensity diagram revealed that the source initially stayed in the low/hard states with two stable flux levels for about three months, and then moved into the high/soft state (Paper I). A radio flare was detected simultaneously with the spectral transition (Negoro et al. 2010; Brocksopp et al. 2010), and the proper motion of the jet ejecta was later found with VLBI observations (Yang et al. 2010). Miller-Jones et al. (2011) identified it as an approaching jet ejected coincidently with the X-ray state transition. From the observed flux of the approaching jet and its upper limit of the receding one, they constrained the jet speed and the inclination angle from the line-of-sight to be $> 0.66c$ and $< 49°$, respectively, by assuming that the axes of the twin jets are aligned. Shaposhnikov et al. (2010) estimated the black hole mass and distance to be $9.6 \pm 0.9\,M_\odot$ and 3.5 ± 0.4 kpc, respectively, using the spectral–timing correlation technique (Shaposhnikov & Titarchuk 2009). However, the compact object mass has not been estimated via an optical mass-function technique. To firmly establish the nature of XTE J1752−223, however, it is quite important to constrain the black hole mass by an independent approach.

In this paper, we present the results from a detailed spectral analysis of XTE J1752−223 utilizing the MAXI/GSC data, together with those of Swift/XRT and Suzaku, mainly focusing on the spectra in the high/soft state. We then discuss the constraints on the black hole mass and distance based on our results. In the Appendix, we present the current status of spectral calibration of the MAXI/GSC using the Crab Nebula, which is fully reflected in this paper and in a similar work for the black hole candidate GX 339−4 reported by Shidatsu et al. (2011b). The spectral fitting was carried out on XSPEC version 12.6. Errors are quoted at statistical 90% confidence limits for a single parameter throughout the paper.

2. MAXI Observations and Analysis

2.1. MAXI Observations

The first astronomical mission on the International Space Station (ISS), MAXI, has been operating since 2009 August. The payload carries two kinds of X-ray all-sky monitors: the Gas-Slit Camera (GSC: Mihara et al. 2011) and the Solid-state Slit Camera (SSC: Tsunemi et al. 2010; Tomida et al. 2011). The GSC consists of Xe-gas proportional counters for the X-ray detector and slat collimators with a slit to localize the direction of the incident X-rays. The counters employ resistive-carbon wires for detector anodes to determine the X-ray position along the anode wire. Twelve identical units (referred to as GSC_0, ..., GSC_9, GSC_A, and GSC_B) are assembled so that they instantaneously cover two rectangular field of views (FoVs) of $3° \times 160°$ with an equal area.

After the operation started in 2009 August, two counters, GSC_6 and GSC_9, were stopped on 2009 September 8 and 14, respectively, for high-voltage breakdown. Two other counters on GSC_A and GSC_B were stopped temporarily on September 23, because diagnostic data indicated that they may also break down rather soon. Consequently, the outburst of XTE J1752−223 from 2009 October to 2010 June was covered by eight GSC camera units out of the twelve.

The GSC FoV is limited by slats collimators. The visibility for a target at a given sky position changes according to the ISS orbital motion; hereafter, we call the visibility time as "transit". Each transit lasts for 40–150 s, and the effective area of each GSC counter changes due to the triangular-shaped collimator transmission function, with a peak value of 4–5 $\rm cm^2$. The MAXI/GSC scanned the direction of XTE J1752−223 2041 times in total from the discovery on 2009 October 23 (MJD 55127) to 2010 June 3 (MJD 55350). The total exposure times effective area becomes 534.8 $\rm cm^2$ ks.

2.2. Analysis

For data analysis, we used the MAXI specific analysis tools, which were developed by the MAXI team. We analyzed the GSC event data version 0.3b, which include the data taken by counters operated at the nominal high voltage (= 1650 V), but excluding those of anode #1 and #2, whose energy responses have not yet been sufficiently calibrated. We discarded events taken while the GSC FoVs were interfered by the solar panels

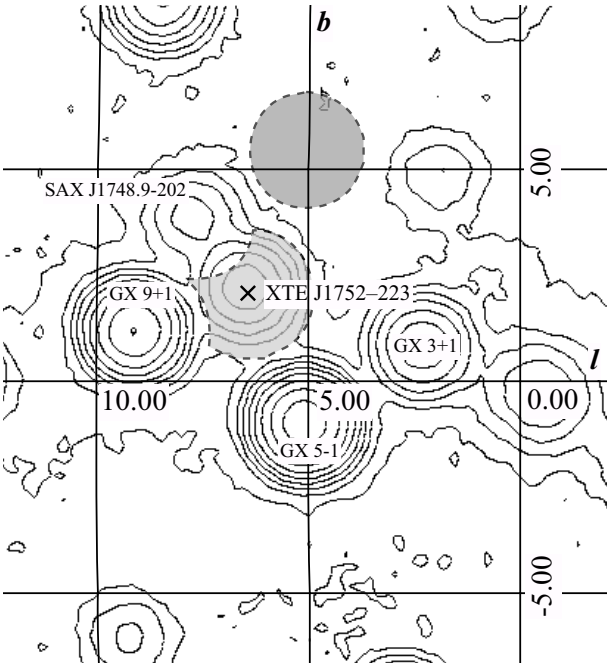

Fig. 1. 2–20 keV MAXI/GSC image in the Galactic coordinate around XTE J1752−223. The data are accumulated from MJD 55200 to MJD 55299. The intensity contours are shown by a log scale. The source and background regions for the analysis are indicated by the shadowed regions.

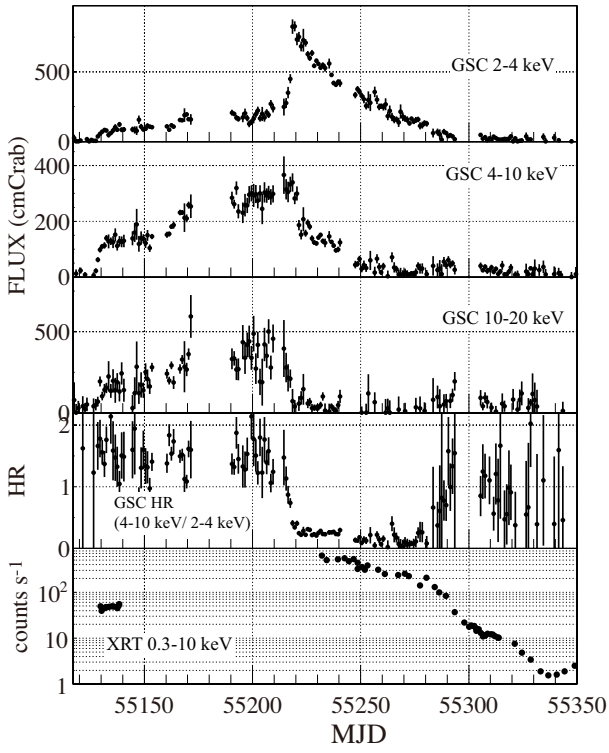

Fig. 2. MAXI/GSC and Swift/XRT light curves of XTE J1752−223 in the 2009–2010 outburst. Four panels from the top show the GSC light curves in three energy bands of 2–4, 4–10, and 10–20 keV, and the hardness ratio between the 4–10 keV and 2–4 keV bands. The bottom shows the Swift/XRT light curve in the 0.3–10 keV band.

and other ISS payloads. The events detected at the anode-end area were also screened since the background is higher therein. These event were cut with a condition that the photon incident angle ($\phi_{\rm col}$; see Mihara et al. 2011 for the definition) is higher than 36°. As shown in figure 1, we carefully extracted events for the source and the background from circular regions with a 1.°5 radius, excluding regions within 1.°7 of nearby sources, GX 5−1, GX 9+1, and SAX J1748.9−2021 in NGC 6440. We used only those data when the source and background regions were both fully scanned in a transit.

We performed spectral analysis of the data taken between MJD = 55200 and MJD = 55293, during which both the "hard-to-soft" and "soft-to-hard" transitions took place (Paper I). The net effective exposure was 194.5 $\rm cm^2$ ks for 752 transits. We divided the whole dataset into groups with typical lengths of a few days so that the spectrum in each group would have sufficient photon statistics, except for the epoch around the "hard-to-soft" state transition when the spectrum changed rapidly. Eventually, data were separated into 49 groups whose exposures times effective area were 0.2–12 $\rm cm^2$ ks. The energy response matrix for each group was calculated by the response builder (Sugizaki et al. 2011). The validity of the energy response was verified using the Crab Nebula (see the Appendix).

2.3. Light Curves during the 2009–2010 Outburst

Figure 2 shows the MAXI/GSC light curves of XTE J1752−223 during the 2009–2010 outburst in the 2–4 keV, 4–10 keV, and 10–20 keV bands, together with the hardness ratio between the 4–10 keV and 2–4 keV bands. They were updated from those presented in Paper I, after applying the latest calibration and the same data screening as used for the spectral analysis (subsection 2.4 and the Appendix). The MAXI/GSC first detected XTE J1752−223 at 15:05 (UT) on 2009 October 23 (MJD 55127) when the 2–20 keV X-ray intensity was 30 mCrab. It monitored the source almost uniformly, except for the time when the FoV was close to the Sun (MJD 55154–55159 and MJD 55172–55188) and when the poles of the scanning axis were close to the source (around MJD 55300). The light curves reveal that the source stayed in the initial low/hard state for an extraordinary long period of about 3 months, and took two flux-plateau phases in the meantime (Paper I).

The "hard-to-soft" state transition occurred on MJD 55218, and the following behavior agrees well with those of the typical BHC outbursts (Remillard & McClintock 2006). The X-ray intensity was peaked at 420 mCrab on 2010 January 22 (MJD 55218), then decayed exponentially with an e-folding time of 34 d through the high/soft state. The "soft-to-hard" transition started on 2010 March 30 (MJD 55285), and then the source returned to the low/hard state on 2010 April 6 (MJD 55292). On 2010 June 28 (MJD 55375), the source flux fell below the MAXI/GSC detection sensitivity per day (20 mCrab). Thus, the total duration of the outburst became about eight months.

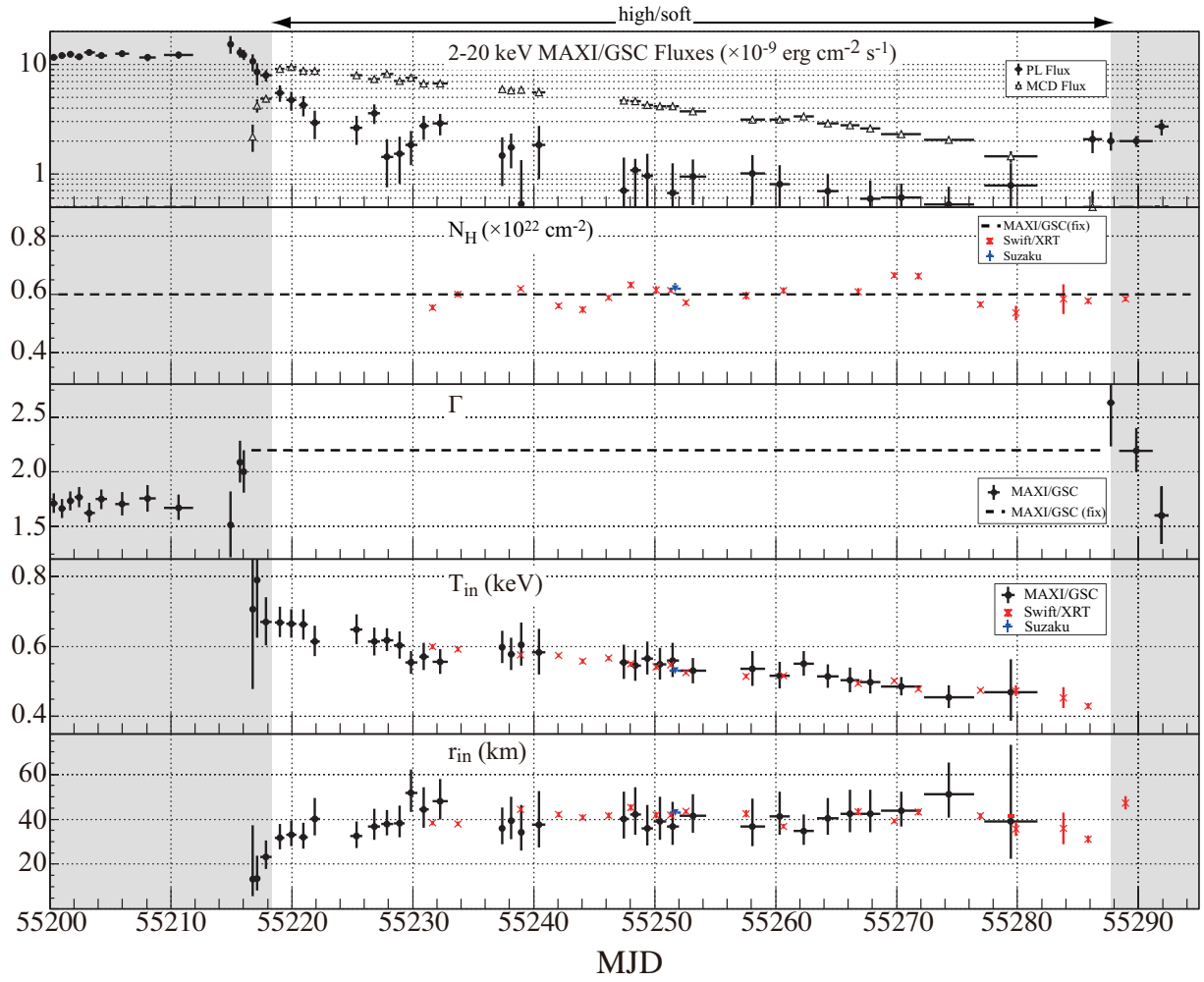

Fig. 3. Evolution of the spectral parameters of XTE J1752−223. The MAXI/GSC, Swift/XRT, and Suzaku results using the MCD plus power-law model are shown by black, red (cross), and blue (inverse triangle) points, respectively. From top to bottom panels, 2–20 keV fluxes of MCD and power-law components, the hydrogen column density, $N_{\rm H}$, the photon index, Γ, the innermost temperature, $T_{\rm in}$, and the innermost radius, $r_{\rm in}$, are indicated.

2.4. *Spectral Analysis*

For the spectral analysis, we employed the standard model for BHCs in the high/soft state, a multi-color disk (MCD; diskbb in XSPEC) model plus a power-law representing the hard tail. The wabs (Morrison & McCammon 1983) model with solar abundances by Anders and Ebihara (1982) was applied for the interstellar absorption. The hydrogen column density ($N_{\rm H}$) toward XTE J1752−223 was fixed at $0.6 \times 10^{22}\,{\rm cm}^{-2}$, based on the Swift and Suzaku results, as described below. The model has four parameters: the innermost temperature, $T_{\rm in}$, and innermost radius, $r_{\rm in}$,[1] for the MCD component, with the photon index Γ and normalization at 1 keV for the power-law component. We first applied the model to all data. When the MCD component was found to not be necessary (i.e., the 90% confidence range of the MCD normalization contains zero), only the power-law model was applied with its Γ set free. When the MCD component was required, we fixed $\Gamma = 2.2$ for all of the spectra, because it is often difficult to determine from individual spectrum due to poor statistics and the limited energy coverage of the MAXI/GSC. This photon index corresponds to a typical value obtained when the power-law component is relatively strong ($> 50\%$ of the total flux in the 2–20 keV band). Although Shaposhnikov et al. (2010) suggested from the RXTE/PCA data that the power-law slope is variable between $\Gamma \approx 1.6$–2.2 by using a spectral model different from ours, we confirmed that the varying Γ value within this range only changes the best-fit MCD normalization by $< 3\%$, and hence does not affect our conclusions.

The MCD plus power-law model or single power-law model gave good fits for all MAXI/GSC data. Table 1 summarizes the obtained spectral parameters, while figure 3 plots the evolution of the model parameters. Figure 4 shows typical response-unfolded νF_ν spectra, together with their best-fit models.

The spectra during MJD 55200–55214 (DataID = 1–10) required no MCD component. The photon indices and fluxes were almost constant, meanwhile, at ≈ 1.7 and $1.2 \times 10^{-8}\,{\rm erg\,cm^{-2}\,s^{-1}}$, respectively. On MJD 55215.64–55216.15 (DataID = 11–12), the spectrum dramatically softened to

[1] $r_{\rm in} = \sqrt{N_{\rm diskbb}}\,(D/10\,{\rm kpc})\,(\cos i)^{-1/2}$, where $N_{\rm diskbb}$ is the normalization of the diskbb model. The distance to the source of $D = 3.5$ kpc and inclination angle $i = 0$ are assumed.

Table 1. Best-fit parameters of MAXI observations.

DataID	MJD start–end	Exposure (cm^2 ks)	Γ	Power-law flux*	T_{in} (keV)	r_{in} (km)	Disk flux*	χ^2_ν/dof
1	55200.03–55200.66	3.42	1.71 ± 0.09	11.6 ± 0.7	—	—	—	1.33 (59)
2	55200.73–55201.30	3.41	1.67 ± 0.09	12.1 ± 0.7	—	—	—	1.36 (61)
3	55201.42–55202.00	3.42	1.73 ± 0.09	12.4 ± 0.7	—	—	—	0.92 (64)
4	55202.06–55202.76	3.41	1.77 ± 0.09	11.8 ± 0.7	—	—	—	0.79 (60)
5	55202.82–55203.71	3.41	1.63 ± 0.09	13.0 ± 0.7	—	—	—	0.81 (65)
6	55203.77–55204.72	3.40	1.75 ± 0.09	12.1 ± 0.7	—	—	—	0.93 (62)
7	55205.42–55206.56	2.37	1.70 ± 0.11	12.6 ± 0.8	—	—	—	1.10 (47)
8	55207.38–55208.73	2.01	$1.76^{+0.13}_{-0.12}$	11.6 ± 0.9	—	—	—	0.57 (36)
9	55209.41–55211.84	2.01	$1.67^{+0.12}_{-0.11}$	12.2 ± 0.9	—	—	—	1.13 (39)
10	55214.88–55214.94	0.24	$1.51^{+0.31}_{-0.30}$	$15.4^{+2.9}_{-2.8}$	—	—	—	0.67 (4)
11	55215.64–55215.83	0.83	2.09 ± 0.19	13.0 ± 1.3	—	—	—	0.55 (18)
12	55215.89–55216.15	0.83	$2.00^{+0.20}_{-0.19}$	$12.3^{+1.4}_{-1.3}$	—	—	—	0.87 (17)
13	55216.65–55216.91	1.06	2.20 (fix)	$10.7^{+1.7}_{-2.0}$	$0.71^{+0.29}_{-0.23}$	$13.3^{+23.9}_{-7.6}$	2.2 ± 0.6	1.09 (24)
14	55216.97–55217.29	1.28	2.20 (fix)	$8.5^{+1.8}_{-2.1}$	$0.79^{+0.19}_{-0.16}$	$13.5^{+10.4}_{-5.2}$	4.2 ± 0.6	0.94 (29)
15	55217.42–55218.37	3.39	2.20 (fix)	$8.0^{+0.9}_{-1.0}$	0.67 ± 0.07	$23.2^{+7.4}_{-5.3}$	4.9 ± 0.4	0.86 (51)
16	55218.62–55219.38	2.93	2.20 (fix)	5.5 ± 1.0	$0.67^{+0.05}_{-0.04}$	$31.8^{+6.3}_{-5.0}$	9.2 ± 0.5	0.73 (42)
17	55219.57–55220.39	3.22	2.20 (fix)	4.7 ± 0.9	0.66 ± 0.04	$33.1^{+6.2}_{-5.0}$	$9.6^{+0.5}_{-0.4}$	0.77 (43)
18	55220.58–55221.35	3.06	2.20 (fix)	4.3 ± 0.9	0.66 ± 0.04	$32.0^{+6.4}_{-5.1}$	8.7 ± 0.4	0.63 (40)
19	55221.54–55222.30	2.27	2.20 (fix)	$3.0^{+0.8}_{-0.9}$	0.61 ± 0.04	$40.1^{+9.3}_{-7.2}$	8.8 ± 0.5	1.11 (33)
20	55224.84–55225.85	3.03	2.20 (fix)	2.6 ± 0.8	0.65 ± 0.04	$32.5^{+6.6}_{-5.2}$	8.0 ± 0.4	1.15 (35)
21	55226.30–55227.31	3.31	2.20 (fix)	3.6 ± 0.7	0.61 ± 0.04	$36.9^{+7.7}_{-6.2}$	7.4 ± 0.4	0.63 (39)
22	55227.37–55228.39	3.53	2.20 (fix)	1.4 ± 0.7	0.62 ± 0.03	$38.0^{+6.2}_{-5.2}$	8.2 ± 0.4	1.13 (33)
23	55228.45–55229.34	3.33	2.20 (fix)	1.5 ± 0.7	0.60 ± 0.04	$38.2^{+7.9}_{-6.2}$	7.1 ± 0.4	1.19 (30)
24	55229.41–55230.36	3.82	2.20 (fix)	1.8 ± 0.6	0.55 ± 0.03	$51.7^{+10.5}_{-8.4}$	7.6 ± 0.3	1.25 (32)
25	55230.55–55231.31	3.40	2.20 (fix)	2.7 ± 0.7	0.57 ± 0.04	$44.3^{+10.1}_{-8.0}$	6.7 ± 0.4	1.29 (34)
26	55231.63–55232.90	4.30	2.20 (fix)	$2.9^{+0.6}_{-0.7}$	$0.56^{+0.04}_{-0.03}$	$48.0^{+10.1}_{-8.1}$	6.8 ± 0.3	0.93 (38)
27	55237.15–55237.62	2.66	2.20 (fix)	1.5 ± 0.7	0.60 ± 0.05	$36.0^{+9.3}_{-7.1}$	6.0 ± 0.4	0.79 (26)
28	55237.87–55238.45	2.84	2.20 (fix)	1.7 ± 0.6	0.58 ± 0.05	$39.3^{+10.8}_{-8.1}$	5.8 ± 0.4	0.96 (27)
29	55238.82–55239.14	1.56	2.20 (fix)	$0.5^{+0.8}_{-0.5}$	0.61 ± 0.06	$34.3^{+12.1}_{-8.4}$	5.9 ± 0.5	1.32 (18)
30	55239.84–55240.99	1.60	2.20 (fix)	1.8 ± 0.9	$0.58^{+0.07}_{-0.06}$	$37.5^{+15.0}_{-10.0}$	5.6 ± 0.5	1.16 (20)
31	55247.06–55247.89	3.22	2.20 (fix)	0.7 ± 0.7	0.55 ± 0.05	$40.2^{+12.0}_{-8.9}$	4.7 ± 0.3	0.73 (23)
32	55247.95–55248.84	3.24	2.20 (fix)	$1.1^{+0.3}_{-0.6}$	$0.55^{+0.05}_{-0.04}$	$42.1^{+12.1}_{-9.0}$	4.6 ± 0.3	0.61 (24)
33	55248.91–55249.86	3.17	2.20 (fix)	1.0 ± 0.6	0.57 ± 0.05	$36.0^{+10.4}_{-7.7}$	4.2 ± 0.3	0.92 (24)
34	55249.92–55250.94	3.32	2.20 (fix)	0.5 ± 0.5	$0.55^{+0.05}_{-0.04}$	$39.1^{+11.1}_{-8.3}$	4.2 ± 0.3	0.96 (21)
35	55251.00–55252.02	3.22	2.20 (fix)	0.7 ± 0.6	0.56 ± 0.05	$36.7^{+11.0}_{-8.0}$	4.2 ± 0.3	0.41 (23)
36	55252.08–55254.24	5.51	2.20 (fix)	0.9 ± 0.4	$0.53^{+0.04}_{-0.03}$	$41.6^{+9.7}_{-7.6}$	3.7 ± 0.2	0.84 (28)
37	55257.09–55259.12	3.83	2.20 (fix)	1.0 ± 0.5	0.54 ± 0.05	$36.9^{+12.5}_{-8.9}$	3.1 ± 0.2	0.66 (23)
38	55259.52–55261.16	6.53	2.20 (fix)	0.8 ± 0.4	0.52 ± 0.04	$41.4^{+10.8}_{-8.2}$	3.1 ± 0.2	0.53 (26)
39	55261.49–55263.19	6.82	2.20 (fix)	0.3 ± 0.3	$0.55^{+0.04}_{-0.03}$	$34.7^{+7.6}_{-6.0}$	3.3 ± 0.2	0.99 (27)
40	55263.44–55265.22	8.85	2.20 (fix)	0.7 ± 0.3	0.51 ± 0.03	$40.4^{+9.0}_{-7.1}$	2.9 ± 0.1	0.54 (29)
41	55265.35–55266.94	8.52	2.20 (fix)	0.4 ± 0.3	$0.50^{+0.04}_{-0.03}$	$42.4^{+10.6}_{-8.1}$	2.8 ± 0.1	1.11 (25)
42	55267.00–55268.66	8.37	2.20 (fix)	0.6 ± 0.3	$0.50^{+0.04}_{-0.03}$	$42.4^{+10.6}_{-8.2}$	2.6 ± 0.1	0.94 (27)
43	55268.72–55272.02	16.93	2.20 (fix)	0.6 ± 0.2	0.49 ± 0.03	$43.7^{+8.5}_{-6.9}$	2.3 ± 0.1	0.94 (36)
44	55272.28–55276.41	12.51	2.20 (fix)	0.5 ± 0.2	0.46 ± 0.03	$51.3^{+13.9}_{-10.5}$	2.0 ± 0.1	0.72 (29)
45	55277.23–55281.63	3.98	2.20 (fix)	0.8 ± 0.5	$0.47^{+0.09}_{-0.08}$	$39.0^{+34.2}_{-16.6}$	1.4 ± 0.2	0.94 (14)
46	55285.44–55286.97	2.34	2.20 (fix)	$2.1^{+0.4}_{-0.5}$	$0.31^{+0.20}_{-0.14}$	$118.7^{+2179.5}_{-111.7}$	0.5 ± 0.2	0.46 (9)
47	55287.41–55288.05	2.42	$2.63^{+0.47}_{-0.40}$	2.0 ± 0.4	—	—	—	0.39 (9)
48	55288.43–55291.16	8.98	$2.19^{+0.21}_{-0.19}$	2.0 ± 0.2	—	—	—	0.58 (32)
49	55291.35–55292.49	3.41	$1.60^{+0.27}_{-0.26}$	$2.7^{+0.5}_{-0.4}$	—	—	—	0.61 (14)

* In units of 10^{-9} erg s^{-1} cm^{-2} (2–20 keV).

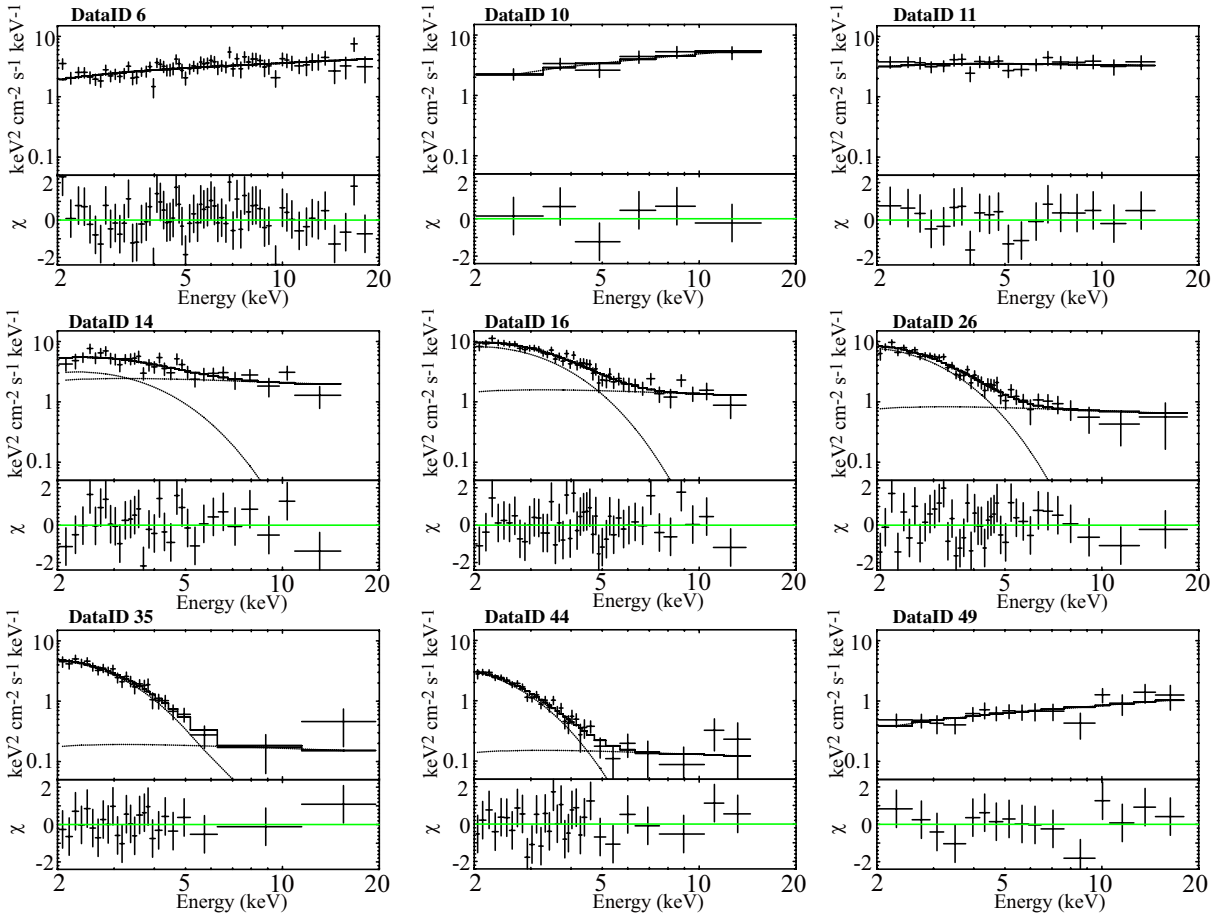

Fig. 4. Examples of the νF_ν spectrum of XTE J1752−223 observed with the MAXI/GSC together with the best-fit models. The panels correspond to DataIDs 6, 10, 11, 14, 16, 26, 35, 44, and 49. DataID 35 was taken approximately at the same time as the Suzaku observation.

$\Gamma \sim 2.0$. The MCD component then appeared after MJD 55216.65 (DataID = 13), and lasted until MJD 55286 (DataID = 46), although the power-law flux was dominant over MJD 55216.65–55218.37 and on MJD 55286.97 in the 2–20 keV band. The MCD flux reached a peak of $\sim 1 \times 10^{-8}$ erg s^{-1} cm^{-2} on 2010 January 23 (MJD 55219), and then decreased. The innermost temperature, $T_{\rm in}$, gradually decreased from $\sim$0.7 keV to $\sim$0.4 keV toward MJD 55286.97. In contrast, the innermost radius $r_{\rm in}$ was almost constant at $\sim$41 km (for $D = 3.5$ kpc and $i = 0°$) then, except for the epoch before the state transition on MJD 55218.37 (DataID = 13–15).

Based on these results, we identified that the source was likely to be in the low/hard state before MJD 55214, the intermediate state over MJD 55215–55218, the high/soft state over MJD 55219–55282, and then came back to the low/hard state after MJD 55292 through the intermediate state between MJD 55285 and 55292. For later discussions, we calculated the weighted average of $r_{\rm in}$ in the high/soft state to be 41.0 ± 2.1 km, using the observations on MJD 55230–55282 when the contribution of the power-law component was sufficiently small.

As Steiner et al. (2009) pointed out, the initial variation of $r_{\rm in}$ observed on MJD 55216–55218 in the intermediate state may have been caused by ignoring the Comptonized photons in the calculation of $r_{\rm in}$. In these epochs, the fraction of the power-law component was $>50\%$ of the total X-ray flux in the 2–20 keV band, and hence the Compton up-scattering of the disk blackbody emission can significantly reduce the normalization of the direct MCD component (McClintock et al. 2009). We find it difficult, however, to obtain a reliable estimate of the innermost radius corrected for this effect from the MAXI/GSC data alone, which strongly couples with the photon index of the Compton scattered component. We leave any detailed investigation of the spectra in the intermediate state for future work, and concentrate on those in the high/soft state in the following analysis.

3. Swift Observations and Analysis

From 2009 October 25 to 2010 July 29, the Swift/XRT (Burrows et al. 2005) carried out 67 pointing observations of XTE J1752−223 in the Windowed Timing (WT) mode. Due to the Sun angle constraint, the observations were interrupted between 2009 November 4 (MJD 55139) and 2010 February 3 (MJD 55230). We analyzed data of 17 observations taken in the high/soft state after 2010 February 4 (MJD 55231). All of the XRT spectra and light curves were produced by the

Table 2. Best-fit parameters of Swift/XRT observations.*

ObsID	MJD start	Exposure (s)	$N_{\rm H}$ ($\times 10^{22}\,{\rm cm}^{-2}$)	Power-law flux†	$T_{\rm in}$ (keV)	$r_{\rm in}$ (km)	Disk flux†	χ^2_ν/dof
00031532010	55231.6	1374.3	0.56 ± 0.01	2.34 ± 0.23	0.60 ± 0.01	$38.4^{+1.1}_{-1.0}$	5.66 ± 0.20	1.68 (224)
00031532011	55233.7	1595.0	0.60 ± 0.01	2.40 ± 0.19	0.59 ± 0.01	38.0 ± 1.0	5.39 ± 0.14	1.29 (238)
00031532012	55238.9	2360.7	0.62 ± 0.01	1.26 ± 0.11	0.58 ± 0.01	$44.3^{+0.8}_{-0.7}$	6.39 ± 0.11	1.50 (244)
00031532014	55242.0	1421.4	0.56 ± 0.01	2.41 ± 0.19	0.57 ± 0.01	42.2 ± 1.1	5.21 ± 0.15	1.64 (234)
00031532015	55244.0	1123.8	0.55 ± 0.01	1.07 ± 0.17	0.56 ± 0.01	$40.9^{+1.3}_{-1.2}$	$4.31^{+0.17}_{-0.16}$	1.22 (191)
00031532016	55246.2	1411.8	0.59 ± 0.01	2.80 ± 0.18	0.57 ± 0.01	41.7 ± 1.1	$4.79^{+0.13}_{-0.12}$	1.56 (241)
00031532018	55248.0	835.6	0.63 ± 0.01	1.29 ± 0.16	0.55 ± 0.01	45.3 ± 1.4	$5.01^{+0.14}_{-0.13}$	0.95 (202)
00031532019	55250.1	1144.3	0.61 ± 0.01	0.47 ± 0.12	0.54 ± 0.01	41.7 ± 1.4	$3.96^{+0.16}_{-0.14}$	1.22 (177)
00031532020	55251.3	3026.5	0.61 ± 0.01	0.87 ± 0.07	0.55 ± 0.01	41.9 ± 0.7	4.07 ± 0.07	1.62 (238)
00031532021	55252.6	1524.0	0.57 ± 0.01	0.65 ± 0.09	0.53 ± 0.01	43.4 ± 1.1	3.80 ± 0.06	1.50 (193)
00031640001	55257.6	890.9	0.60 ± 0.01	0.69 ± 0.11	0.52 ± 0.01	$42.5^{+1.6}_{-1.5}$	3.05 ± 0.08	1.22 (174)
00031640002	55260.7	909.9	0.61 ± 0.01	0.25 ± 0.05	0.52 ± 0.01	$36.9^{+1.1}_{-1.0}$	$2.23^{+0.09}_{-0.08}$	1.34 (180)
00031640003	55266.8	1209.8	0.61 ± 0.01	0.17 ± 0.06	0.50 ± 0.01	$43.4^{+1.5}_{-1.4}$	2.38 ± 0.09	1.25 (161)
00031640004	55269.8	1184.1	0.67 ± 0.01	0.32 ± 0.04	0.50 ± 0.01	$39.3^{+1.0}_{-0.9}$	2.00 ± 0.05	1.61 (197)
00031640005	55271.8	1214.6	0.66 ± 0.01	0.33 ± 0.04	0.48 ± 0.01	43.3 ± 1.3	1.75 ± 0.06	1.41 (181)
00031640006	55276.9	977.8	0.57 ± 0.01	0.34 ± 0.04	0.48 ± 0.01	$41.5^{+1.2}_{-1.1}$	1.67 ± 0.04	1.34 (177)
00031640007	55279.8	128.3	$0.54^{+0.03}_{-0.02}$	±0.12	0.47 ± 0.01	$35.8^{+3.1}_{-2.8}$	$0.99^{+0.11}_{-0.10}$	1.00 (108)

* Photon indices were fixed to 2.20.
† In units of $10^{-9}\,{\rm erg\,s^{-1}\,cm^{-2}}$ (2–20 keV).

web interface (Evans et al. 2009) supplied by the UK Swift Science Data Centre at the University of Leicester. We used the XRT response matrix file for the WT mode version 12. All of the 17 observations with an exposure time of a few ks each were analyzed independently.

The first results of the Swift/XRT spectral analysis were already reported by Curran et al. (2011). They employed the same MCD plus power-law model as we used in the MAXI/GSC analyses, but derived a different result: that the innermost radius changed significantly with time. The difference is considered to come from the fact that they left the power-law index free and obtained a wide range of Γ between ~0 and ~3, even though this quantity is not constrained when the MCD component is strong. Hence, we reanalyzed the XRT spectra by fixing Γ at 2.2, the same value as adopted for the MAXI/GSC spectra. The $N_{\rm H}$ was left free because the Swift/XRT is sensitive down to ~0.3 keV. The resultant parameters are summarized in table 2, which are also plotted in figure 3. The values of $r_{\rm in}$ were thus constant, with at most a 5% scatter around the weighted mean of $r_{\rm in}=41.4\pm0.3$ km.

4. Suzaku Observations and Results

4.1. Observation

We also observed XTE J1752−223 in the high/soft state with Suzaku (Mitsuda et al. 2007) as a Target-of-Opportunity (ToO) from 2010 February 24 (MJD 55251) 04:58:00 to February 25 04:27:24 (ObsID: 904005010). Suzaku carries 4 X-ray telescope modules (XRT: Serlemitsos et al. 2007), each with a focal-plane X-ray CCD imager consisting the XIS (X-ray Imaging Spectrometer: Koyama et al. 2007) covering the 0.2–12 keV energy band. Since XIS 2 has not been available, the two remaining front-illuminated (FI) CCDs (XIS 0 and XIS 3) were operated for this observation together with the back-illuminated (BI) CCD (XIS 1). The three XIS cameras were operated with burst and window options. The burst time, window size, and editing mode were "0.3 s, 1/4 window, and 2×2" for XIS 0 and XIS 3, and "0.1 s, normal window, and 3×3" for XIS 1, respectively. The Hard X-ray Detector (HXD: Takahashi et al. 2007; Kokubun et al. 2007), covering the 10–70 keV energy band with Si PIN photo-diodes (HXD-PIN), and the 50–600 keV range with GSO scintillation counters (HXD-GSO), was operated in the normal mode. The source was observed at the HXD nominal position.

4.2. Data Reduction

The data reduction and analyses were performed using Suzaku FTOOLS in HEASOFT version 6.10 provided by the NASA/GSFC Suzaku GOF. All of the XIS and HXD data were reprocessed by the Suzaku pipeline processing version 2.4.12.27, with the latest calibration database (CALDBVER) hxd20090902, xis20090925, and xrt20080709.

The image degradation due to "thermal wobbling" of the satellite pointing was corrected by using the attitude file updated with AEATTCOR2. We screened the XIS data under the standard criteria, and discarded events during time intervals when the telemetry of the XIS was saturated. The resultant net exposure was 10.6 ks and 449 s for FIs and BI, respectively. The BI exposure was short, because the 0.1 s burst time with a normal window makes the exposure 0.1 s in an 8 s-period, and

the exposure is one twelfth of each FI's exposure. Furthermore, the fraction of out-of-time events (Koyama et al. 2007) is more significant in the BI data, which would introduce systematic uncertainties in the spectral analysis. Hence, we did not use the XIS 1 data in this paper. The average 0.5–10 keV count rate was $\sim$400 counts s^{-1} and $\sim$700 counts s^{-1} with FIs and BI, respectively. We extracted the XIS 0 and 3 events from a rectangle region of 8.′6 × 4.′5 tracing the 1/4 window area centered on the image peak, and the background from another region avoiding contaminating point sources. The source was so bright that the XIS suffered from photon pileup at the image center. Using the software of AEPILEUPCHECKUP (Yamada et al. 2012), which automatically detects the extent of pileup utilizing radial surface brightness profiles and other sets of information, we excluded a circular region within 1.′5 of the image peak for XIS 0 and 3, to extract the events whose pileup fraction is below 1%. We combined the spectra and response files of the two FI cameras to increase the photon statistics in the spectra. To account for possible uncertainties in the instrument calibration (e.g. Makishima et al. 2008), systematic errors of 1% were assigned to each energy bin of the XIS spectra.

We obtained the cleaned HXD events with the standard criteria. After a dead-time correction, the net exposures of PIN and GSO were 21.2 and 27.0 ks, respectively. The dead-time fraction was 18.2% and 7.5% for PIN and GSO, respectively. The cosmic X-ray background (CXB) was modeled while assuming an exponentially cutoff power-law model (Boldt 1987). The non-X-ray background (NXB) model is provided by the HXD team (Fukazawa et al. 2009). We used the model with METHOD = "LCFITDT(bgd_d)", and the version of METHODV = "2.0ver0804" and "2.4ver0912-64" for the data of PIN and GSO, respectively. After subtracting the modeled NXB and CXB, the source signals were significantly detected by PIN up to 50 keV, above the systematic uncertainty on the NXB model ($\sim$3%). Since the GSO signals were comparable to the systematic errors of the NXB model therein ($\sim$1%), we consider the source detection with GSO being insignificant.

4.3. *Spectral Analysis*

As shown in figure 5a, we used an energy range of 1.2–10 keV for the XIS spectrum and 15–50 keV for the HXD-PIN spectrum, where the calibrations of the energy responses were well established. The energy bands of 1.6–2.0 keV and 2.2–2.4 keV were excluded so as to avoid large systematic uncertainties of the effective area near the silicon K edge (1.74 keV and 1.84 keV for Kα and Kβ, respectively) and gold M edge (2.29 keV), respectively. In a combined fit to the XIS and HXD-PIN spectra, we employed a cross normalization factor of 1.18 between XIS and PIN (SUZAKU-MEMO-2008-06).

We firstly fitted the spectra with the MCD plus power-law model modified by interstellar absorption (wabs model), the same one as adopted to fit the MAXI/GSC and Swift/XRT spectra in the previous sections. The residuals in units of χ are shown in the figure 5b. The fit was found to be unacceptable (χ^2/dof = 230.1/136), leaving an emission-line feature at $\approx$6.5 keV, and significant broad edge-like residuals above $\sim$7 keV. These features may be explained away by several

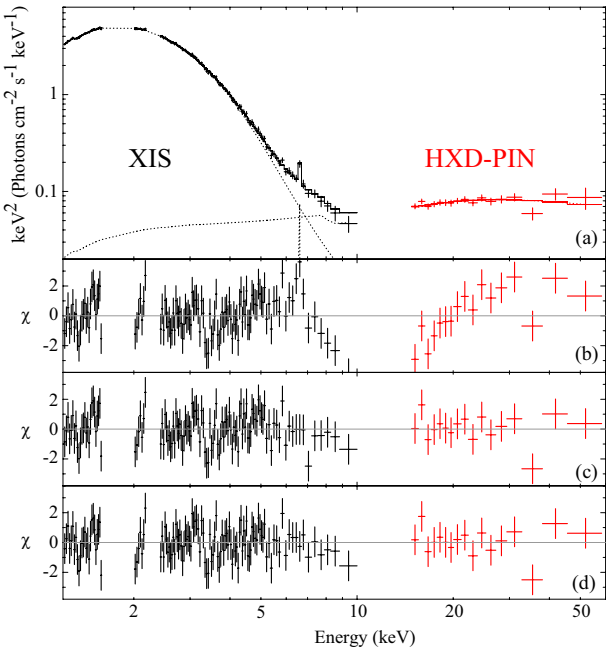

Fig. 5. (a) Suzaku response-unfolded νF_ν spectrum of XTE J1752−223 from the best-fit for wabs × (compPS + pexriv + gaus), and the residuals between the data and best-fit models for (b) wabs × (diskbb + powerlaw), (c) wabs × smedge × (diskbb + powerlaw + gaus), (d) wabs × (compPS + pexriv + gaus).

different approaches; e.g., by invoking a broad Fe-K line concept (Reis et al. 2010) or applying a so-called smeared-edge model (e.g., Ebisawa et al. 1994; Dotani et al. 1997) to account for the edge structure. The latter approach with the wabs × smedge × (diskbb + powerlaw + gaus) model gave an acceptable fit (χ^2/dof = 141.6/133; figure 5c) with a maximum optical depth of $5.50^{+1.4}_{-0.75}$ for fixed edge energy and width of 7.11 keV and 10 keV, respectively. A narrow emission line was found at $E_c = 6.59^{+0.08}_{-0.07}$ keV with a 1 σ line width of 10 eV (fixed) and an equivalent width of $EW = 63^{+42}_{-41}$ eV. These approaches are empirical and may be degenerate, however.

As an alternative possibility, we resorted to the idea of Kolehmainen, Done, and Diaz Trigo (2011) that the disk emission is broader than the simplest MCD model, which could lead to an artificial detection of broad iron-K features. Assuming that weak Comptonization of the MCD emission took place, we replaced the diskbb model with a compPS model (Poutanen & Svensson 1996), which computes Compton scattering by hot corona using an exact numerical solution radiative transfer equation. We chose "slab" (geom = 1) geometry and an MCD spectrum as the seed photons. We left the optical depth of the corona τ as a free parameter, but fixed the electron temperature at T_e = 10 keV and covering fraction at cov_{frac} = 1 to avoid strong coupling between these parameters; the choice of T_e did not affect our results on the disk parameters over the statistical errors. The presence of a fluorescence iron-K line at $\approx$6.6 keV indicates that a reflection continuum must be included in the model as well. Hence, we adopted the pexriv model (Magdziarz & Zdziarski 1995) for the power-law component, which was considered to be the main source of irradiation onto the disk in the high/soft state. The model thus became

Table 3. Best-fit parameters for the Suzaku observation.

Model					
wabs	diskbb/compPS[†]	powerlaw/pexriv[‖]	gaus[**]	smedge[††]	
$N_{\rm H}^{*}$	$T_{\rm in}$ (keV) $r_{\rm in}^{\ddagger}$ (km) $\tau^{\S}$	Γ Norm[#]	$E_{\rm c}$ (keV) EW (eV)	$\tau_{\rm max}^{\ddagger\ddagger}$	χ^2/dof
wabs × (diskbb + powerlaw)					
0.62 ± 0.02	0.53 ± 0.01	2.29 ± 0.06	—	—	230.1/136
—	42.9 ± 0.9	0.16 ± 0.03	—	—	—
—	—	—	—	—	—
wabs × smedge × (diskbb + powerlaw + gaus)					
0.65 ± 0.02	0.526 ± 0.003	2.22 ± 0.05	$6.59^{+0.08}_{-0.07}$	$5.50^{+1.4}_{-0.75}$	141.80/133
—	44.0 ± 1.0	0.16 ± 0.02	63^{+42}_{-41}	—	—
—	—	—	—	—	—
wabs × (compPS + pexriv + gaus)					
0.67 ± 0.02	$0.507^{+0.005}_{-0.006}$	2.13 ± 0.01	$6.60^{+0.08}_{-0.07}$	—	131.4/133
—	47.2 ± 0.8	$0.05^{+0.08}_{-0.04}$	98 ± 43	—	—
—	0.41 ± 0.05	—	—	—	—

* In units of $10^{22}\,{\rm cm}^{-2}$.
† $T_{\rm e}$ and $\mathrm{cov_{frac}}$ are fixed at 10 keV and at 1, respectively. No reflection from the compPS component itself is considered.
‡ $D = 3.5$ kpc and $i = 0°$ are assumed.
§ Optical depth of the corona.
‖ Fixed at $\Omega = 2\pi$, $i = 25°$, and $\xi_{\rm i} = 1000\,{\rm erg\,cm\,s^{-1}}$. No high energy cutoff is set in the incident power-law continuum.
A normalization in units of photons $\rm cm^{-2}\,s^{-1}$ at 1 keV.
** 1σ line width is fixed at 10 eV.
†† The edge energy and width, photo-electric cross-section are fixed at 7.11 keV, 10 keV, and −2.67, respectively.
‡‡ The maximum absorption factor at threshold.

wabs × (compPS + pexriv + gaus) in the XSPEC terminology. For the pexriv component, we assumed no high-energy cutoff, and fixed the solid angle of the reflector at $\Omega = 2\pi$, inclination at 25°, and ionization parameter at $\xi_{\rm i} = 1000\,{\rm erg\,cm\,s^{-1}}$, which consistently explain both the iron-K line intensity and the center energy. The fit was found to be acceptable with $\chi^2/{\rm dof} = 129.9/132$; as shown in figure 5d, the broad edge-like residuals mostly disappeared. The model gave an absorbed 2–20 keV flux of $(3.76\pm0.02)\times10^{-9}\,{\rm erg\,s^{-1}cm^{-2}}$. We obtained $\tau = 0.41\pm0.05$ and $\Gamma = 2.13\pm0.01$ in the pexriv component, a reasonable value in the high/soft state (e.g., Done & Gierliński 2004). More detailed analysis, more advanced disk-emission modeling, and relativistic Fe-K lines, is beyond the scope of this paper, and will be reported elsewhere.

The best-fit parameters of these models are listed in table 3. We note that by replacing the diskbb model with the compPS model, the best-fit value of $r_{\rm in}$ increased by 13%. This is because a spectrum hardened by Comptonization was assumed in the compPS model, an intrinsic temperature $T_{\rm in}$ became lower, leading to an increase in $r_{\rm in}$. While the difference should be regarded as a systematic modeling uncertainty, we confirm that it does not affect our conclusion. The photon index of the hard tail ($\Gamma = 2.13\pm0.01$) is smaller than the result obtained from the same Suzaku data by Reis et al. (2010) ($\Gamma = 2.54^{+0.02}_{-0.11}$), who did not include the 15–20 keV and 45–50 keV bands in fitting the HXD/PIN spectrum.

5. Discussion

We have analyzed the MAXI/GSC, the Swift/XRT, and Suzaku data of XTE J1752−223 in the high/soft state from MJD 55218.62 to 55281.63. The overall continuum spectra were reproduced by the MCD plus power-law model with interstellar absorption. The innermost temperature, $T_{\rm in}$, decreased from ~0.7 keV to ~0.4 keV, while the innermost radius, $r_{\rm in}$, remained constant. By assuming $D = 3.5$ kpc and $i = 0°$, the values of $r_{\rm in}$ derived from the MAXI/GSC, Swift/XRT, and Suzaku data are 41.0 ± 2.1 km, 41.4 ± 0.3 km, and 42.9 ± 0.9 km, respectively. The results from the three instruments are mutually consistent with each other within the statistical errors. For the following discussion, we employ 41.0 ± 2.1 km for $r_{\rm in}$, as determined from the MAXI/GSC, although we also discuss the case when the Suzaku result with the compPS model ($r_{\rm in} = 47.2\pm0.8$ km) is adopted to take into account the possible systematic uncertainty.

Since the value of $r_{\rm in}$ thus estimated is significantly larger than those found in luminous low-mass X-ray binaries (10 km: Mitsuda et al. 1984), the black hole interpretation of XTE J1752−223 (Paper I; Muñoz-Darias et al. 2010) is considerably reinforced. Furthermore, its constancy allows us to identify it with the ISCO in the high/soft state. The stable $r_{\rm in}$ at 41.0 km is supposed to reach the ISCO in the high/soft state. We note that this $r_{\rm in}$ is an "apparent" innermost radius,

and the "realistic" innermost radius ($R_{\rm in}$) should be estimated as $R_{\rm in} = \xi\kappa^2 r_{\rm in}$, where the spectral hardening factor, κ, is 1.7 (Shimura & Takahara 1995) and correction factor for the boundary condition, ξ, is 0.412 (Kubota et al. 1998). The value of κ has been confirmed in recent work on disk models (e.g., Kubota et al. 2010; Done & Davis 2008). When the central object is assumed to be a non-spinning black hole (i.e., Schwarzschild black hole), $R_{\rm in}$ should equal to 6 $R_{\rm g}$. Then, the black hole mass is estimated as

$$M = \frac{c^2 R_{\rm in}}{6G} = 5.51 \pm 0.28 \left(\frac{D}{3.5\ {\rm kpc}}\right) (\cos i)^{-1/2}\, M_\odot. \quad (1)$$

Using the inclination angle $i < 49°$ obtained from radio observations (Miller-Jones et al. 2011), the black hole mass and distance are constrained in the shadowed area shown in figure 6. If we assume the distance to be 3.5 kpc, the mass will be 5.2–7.1 $M_\odot$, and if $D = 10$ kpc, 15.0–20.4 $M_\odot$.

To validate our method to estimate the black hole mass by employing the MCD model which is a simplified approximation of a true disk spectrum, we also performed a spectral fit to the Suzaku spectra using the kerrbb model (Li et al. 2005). This model calculates the X-ray spectrum of a relativistic accretion disk around a rotating black hole by taking into account the innermost boundary condition and the effects of self-irradiation of the disk. Here we fixed the distance at $D = 3.5$ kpc, spin parameter at $a = 0$, and color correction factor at $\kappa = 1.7$ for consistency with the previous discussion. The fit with the wabs × (kerrbb + pexriv) model was not acceptable (χ^2/dof = 215.5/135), leaving similar residuals shown in figure 5b. Thus, we employed the simpl model (Steiner et al. 2009) with a steep photon index fixed at 7.4 to approximately represent weak Comptonization of the disk emission; the model became wabs × (simpl × kerrbb + pexriv + gaus), which was found to give an acceptable fit (χ^2/dof = 129.5/134). The black hole mass derived for $i = 0°$ and $i = 49°$ is $4.98^{+0.28}_{-0.25}\, M_\odot$ and $8.43^{+0.44}_{-0.42}\, M_\odot$, respectively, which differs by ∼20% from the mass presented in equation (1).

From past observations of BHCs and neutron stars, Maccarone (2003) pointed out that the state transition from the high/soft state to the low/hard state occurs at 1%–4% (centered at 2%) of the Eddington luminosity.[2] Judging from the change of the photon index, XTE J1752−223 went back to the low/hard state around MJD 55292 (DataID 49). The bolometric flux at the transition is $F_{\rm trans} = (6.68 \pm 0.83) \times 10^{-9}$ erg cm^{-2} s^{-1}, assuming a cutoff power-law is continuum with $\Gamma = 1.8$ and a cutoff energy of 200 keV. Using the relation $0.01 < L_{\rm trans}/L_{\rm edd} < 0.04$ and $L_{\rm trans} = 4\pi D^2 F_{\rm bol}$, we can further constrain the distance and black hole mass of XTE J1752−223, as illustrated by the hatched region in figure 6. Thus, we can obtain $D = 2.5$–18 kpc and $M = 3.7$–36 $M_\odot$. When we instead use the Suzaku results, $D = 3.0$–20 kpc and $M = 5.3$–44 $M_\odot$ [based on the wabs × (compPS + pexriv + gaus) model] or $D = 2.3$–22 kpc and $M = 3.1$–55 $M_\odot$ [based on wabs × (simpl × kerrbb + pexriv+gaus)] are derived.

Since we obtain $M > 3\, M_\odot$, our method of estimating M assuming a black hole is self consistent. The conclusion

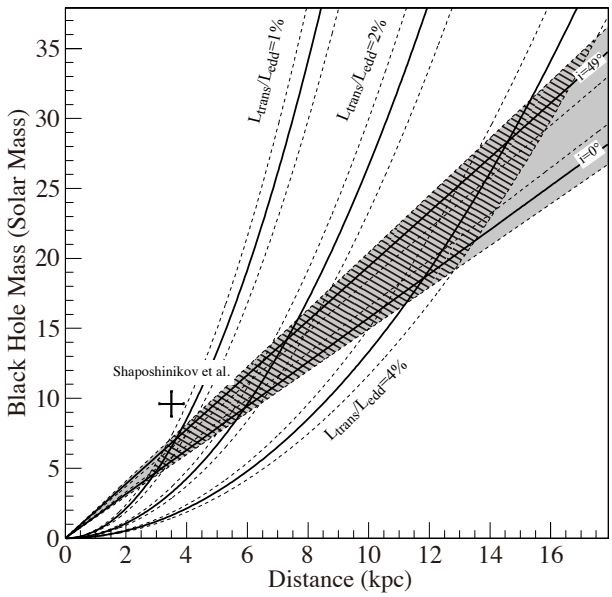

Fig. 6. Observational constraints on the mass and distance of XTE J1752–223. The shadowed region is specified by the innermost radius derived from the MAXI/GSC spectra in combination with the inclination angle $i < 49°$ from the radio observations (Miller-Jones et al. 2011). Each solid line with two dashed lines indicates the best-fit parameter and 90% confidence ranges of flux and $r_{\rm in}$. The hatched region was derived assuming the empirical relation that the soft-to-hard transition occurs at 1%–4% $L_{\rm edd}$.

that the compact object in XTE J1752−223 is a black hole is robust against the assumptions that the rotational axis of the accretion disk and jet axis are exactly aligned, and that the black hole is non-spinning, since the extreme conditions $i = 0°$ and $a = 0$ yield the smallest mass estimate. The values of $M = 9.6 \pm 0.9\, M_\odot$ and $D = 3.5 \pm 0.4$ kpc estimated by Shaposhnikov et al. (2010) are outside the hatched region. If the black hole in XTE J1752−223 is spinning and/or the disk has a larger inclination than 49°, then the discrepancy could be solved.

6. Conclusions

Using data obtained by the MAXI/GSC, the Swift/XRT, and Suzaku, we performed an X-ray spectral analysis of the black hole candidate XTE J1752−223 in the high/soft state. As commonly seen in BHCs, the innermost radius remained constant in this state during the continuous observation with the MAXI/GSC. The results using the MCD plus power-law model were consistent between the three observatories. Detailed spectral modeling using Suzaku data suggests a possibility that the MCD emission may be slightly Comptonized, which could explain the apparently broad iron-K features. Assuming that the innermost radius of the disk corresponds to the ISCO and the black hole is non-spinning, we estimated the mass of the central object as $5.51 \pm 0.28\, M_\odot\, (D/3.5\,{\rm kpc})(\cos i)^{-1/2}$ with corrections for the stress-free inner boundary condition and color hardening factor of 1.7. Furthermore, using the observational results that the inclination angle i is smaller than

[2] $L_{\rm edd} = 1.5 \times 10^{38}\ M/M_\odot$ erg s^{-1} for the solar abundances.

49° from radio observations, and that the "soft-to-hard" transition occurs at 1%–4% Eddington luminosity, the distance and black hole mass of XTE J1752−223 were constrained as 3.1–55 $M_\odot$ and 2.3–22 kpc, respectively, based on an analysis of the Suzaku spectra with a relativistic accretion-disk model. Thus we can conclude that XTE J1752−223 is likely to be a black hole.

This research has made use of MAXI data provided by RIKEN, JAXA, and the MAXI team. Suzaku data is provided by a collaborative mission between the space agencies of Japan (JAXA) and the USA (NASA). We also thank the Swift team for their observation. This work made use of data supplied by the UK Swift Science Data Centre at the University of Leicester. This research was partially supported by the Ministry of Education, Culture, Sports, Science and Technology (MEXT), Grant-in-Aid No.19047001, 20041008, 20540230, 20244015, 20540237, 21340043, 21740140, 22740120. One of the authors (S. N.) is grateful to a grant from the Hayakawa Satio Fund awarded by the Astronomical Society of Japan.

Appendix. MAXI/GSC Spectral Calibration Using the Crab Nebula

We here show the status of the GSC energy response calibration with Crab Nebula data to confirm the validity of the spectral analysis. We used event data with the process version 0.3b, which was screened with the operation high voltage of a nominal 1650 V and anode numbers of #0, #3, #4, and #5, whose positional response had been well established. The event selection was the same as that employed in the first performance verification in Sugizaki et al. (2011).

We here screened the event data with more severe conditions to verify the response calibration with a better accuracy. We selected events taken only during such a good scan transit that the source incident angle, $\phi_{\rm col}$, was $< 36°$, and the area for both the source and the background were completely covered.

The calibration of the energy response was performed using the screened background and Crab Nebula data in the following steps: The energy–Pulse Height Amplitude (PHA) relations, which depend on the detector position along the anode wires, were corrected by a gain factor for each output amplifier. The parameter was calibrated using fluorescent lines in the background spectrum from Ti (4.51 keV) and Cu (8.04 keV) as well as the calibration source ^{55}Fe (5.895 keV). We verified that the gain factor obtained with a 0.1% precision successfully reproduced a gain position dependence within a discrepancy of 1% in RMS throughout the whole detector area. The threshold and the resolution of the Lower-Discriminator (LD) of each amplifier were then calibrated using the Crab Nebula spectra. The LD parameters were tuned such that the results of the spectral fit to an absorbed power-law model would agree with those of the canonical values, photon index $\Gamma = 2.1$ and hydrogen absorption column density $N_{\rm H} = 0.35 \times 10^{22}\,{\rm cm}^{-2}$ (i.e., Toor & Seward 1974; Kirsch et al. 2005).

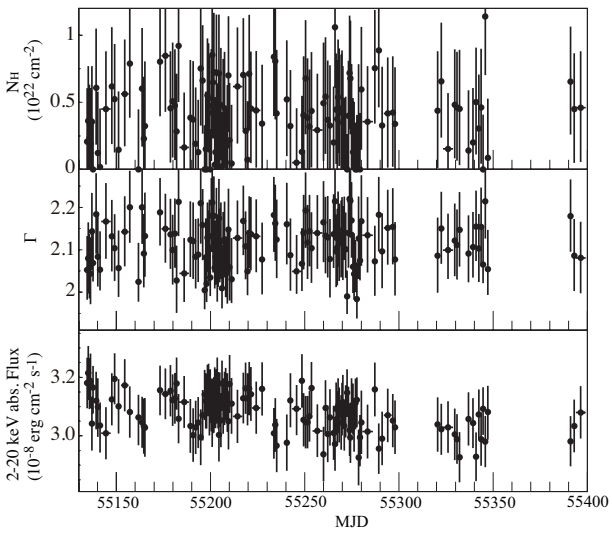

Fig. 7. Best-fit values and statistical errors of the absorbed power-law model to GSC Crab Nebula spectra against the observation time; (top) hydrogen column density, (middle) photon index, (bottom) 2–20 keV absorbed flux.

Table 4. Best-fit values and variations of the absorbed power-law model to GSC Crab Nebula spectra.

Parameter	Canonical	Best fit	rms*
$N_{\rm H}$ ($\times 10^{22}\,{\rm cm}^{-2}$)	0.35	0.39	0.25
Γ	2.10	2.11	0.05
$\Gamma^\dagger$		2.11	0.03
Flux$_{2-20{\rm keV}}{}^\ddagger$	$3.0 \pm 10\%$	3.08	0.06

* Root mean square of the best-fit value.
† $N_{\rm H}$ is fixed at $0.35 \times 10^{22}\,{\rm cm}^{-2}$.
‡ In units of $10^{-8}\,{\rm erg\,s^{-1}cm^{-2}}$.

Figure 7 shows the best-fit parameters to GSC Crab Nebula spectra. The data of multiple scan transits whose total exposure of $> 3.2\,{\rm cm}^2$ ks were grouped so that each spectrum has sufficient photon statistics to constrain the parameters of a power-law model. Table 4 summarizes the results. The derived parameters agree with the canonical values within the statistical errors.

References

Anders, E., & Ebihara, M. 1982, Geochim. Cosmochim. Acta, 46, 2363
Brocksopp, C., Corbel, S., Tzioumis, T., Fender, R., & Coriat, M. 2010, Astron. Telegram, 2400
Boldt, E. 1987, Phys. Rep., 146, 215
Burrows, D. N., et al. 2005, Space Sci. Rev., 120, 165
Curran, P. A., Maccarone, T. J., Casella, P., Evans, P. A., Landsman, W., Krimm, H. A., Brochsopp, C., & Still, M. 2011, MNRAS, 410, 541
Done, C., & Davis, S. W. 2008, ApJ, 683, 389

Done, C., & Gierliński, M. 2004, Prog. Theor. Phys., Suppl., 155, 9
Dotani, T., et al. 1997, ApJ, 485, L87
Ebisawa, K., et al. 1994, PASJ, 46, 375
Evans, P. A., et al. 2009, MNRAS, 397, 1177
Fukazawa, Y., et al. 2009, PASJ, 61, S17
Grove, J. E., Strickman, M. S., Matz, S. M., Hua, X.-M., Kazanas, D., & Titarchuk, L. 1998, ApJ, 502, L45
Kirsch, M. G., et al. 2005, Proc. SPIE, 5898, 22
Kolehmainen, M., Done, C., & Diaz Trigo, M. 2011, MNRAS, 416, 311
Kokubun, M., et al. 2007, PASJ, 59, S53
Koyama, K., et al. 2007, PASJ, 59, S23
Kubota, A., Done, C., Davis, S. W., Dotani, T., Mizuno, T., & Ueda, Y. 2010, ApJ, 714, 860
Kubota, A., Tanaka, Y., Makishima, K., Ueda, Y., Dotani, T., Inoue, H., & Yamaoka, K. 1998, PASJ, 50, 667
Li, L.-X., Zimmerman, E. R., Narayan, R., & McClintock, J. E. 2005, ApJS, 157, 335
Maccarone, T. J. 2003, A&A, 409, 697
Magdziarz, P., & Zdziarski, A. A. 1995, MNRAS, 273, 837
Makishima, K., et al. 2008, PASJ, 60, 585
Makishima, K., Maejima, Y., Mitsuda, K., Bradt, H. V., Remillard, R. A., Tuohy, I. R., Hoshi, R., & Nakagawa, M. 1986, ApJ, 308, 635
Markwardt, C. B., et al. 2009, Astron. Telegram, 2258
Matsuoka, M., et al. 2009, PASJ, 61, 999
McClintock, J. E., Remillard, R. E., Rupen, M. P., Torres, M. A. P., Steeghs, D., Levine, A. M., & Orosz, J. A. 2009, ApJ, 698, 1398
Mihara, T., et al. 2011, PASJ, 63, S623
Miller-Jones, J. C. A., Jonker, P. G., Ratti, E. M., Torres, M. A. P., Brocksopp, C., Yang, J., & Morrell, N. I. 2011, MNRAS, 415, 306
Mitsuda, K., et al. 1984, PASJ, 36, 741
Mitsuda, K., et al. 2007, PASJ, 59, S1
Morrison, R., & McCammon, D. 1983, ApJ, 270, 119
Muñoz-Darias, T., Motta, S., Pawar, D., Belloni, T. M., Campana, S., & Bhattacharya, D. 2010, MNRAS, 404, L94
Nakahira, S., et al. 2009, Astron. Telegram, 2259
Nakahira, S., et al. 2010, PASJ, 62, L27 (Paper I)
Negoro, H., et al. 2010, Astron. Telegram, 2396
Poutanen, J., & Svensson, R. 1996, ApJ, 470, 249
Reis, R. C., et al. 2010, MNRAS, 410, 2497
Remillard, R. A., & McClintock, J. E. 2006, ARA&A, 44, 49
Serlemitsos, P. J., et al. 2007, PASJ, 59, S9
Shakura, N. I., & Sunyaev, R. A. 1973, A&A, 24, 337
Shaposhnikov, N., Markwardt, C., Swank, J., & Krimm, H. 2010, ApJ, 723, 1817
Shaposhnikov, N., & Titarchuk, L. 2009, ApJ, 699, 453
Shidatsu, M., et al. 2011a, PASJ, 63, S785
Shidatsu, M., et al. 2011b, PASJ, 63, S803
Shimura, T., & Takahara, F. 1995, ApJ, 445, 780
Steiner, J. F., Narayan, R., McClintock, J. E., & Ebisawa, K. 2009, PASP, 121, 1279
Sugizaki, M., et al. 2011, PASJ, 63, S635
Takahashi, T., et al. 2007, PASJ, 59, S35
Takahashi, H., et al. 2008, PASJ, 60, S69
Tanaka, Y., & Shibazaki, N. 1996, ARA&A, 34, 607
Tomida, H., et al. 2011, PASJ, 63, 397
Toor, A., & Seward, F. D. 1974, AJ, 79, 995
Tsunemi, H., Tomida, H., Katayama, H., Kimura, M., Daikyuji, A., Miyaguchi, K., Maeda, K., & the MAXI team 2010, PASJ, 62, 1371
Yamada, S., et al. 2012, PASJ, 64 in press
Yang, J., Brocksopp, C., Corbel, S., Paragi, Z., Tzioumis, T., & Fender, R. P. 2010, MNRAS, 409, L64